

On the Impact of the Number of Tiles and Partitioning of RISs on the Maximum Achievable Intensity

Fadil Habibi Danufane*, Ashif Aminulloh Fathnan, R. Priyo Hartono Adji, Arie Setiawan, Prasetyo Putranto

*Research Center for Telecommunications
National Research and Innovation Agency Republic of Indonesia
KST Samaun Samadikum, Jl. Cisitno No.21/154D
Bandung, Indonesia*

Abstract

Reconfigurable intelligent surface (RIS) is a key technology to enable the concept of a smart radio environment (SRE), which is envisioned to meet the ever-increasing demands of connectivity in the upcoming decade. However, most existing works consider an RIS that is seen as a whole surface. However, most existing works consider an RIS that is seen as a whole surface. In this paper, we study the performance of an RIS that consists of multiple tiles, each of which is capable of performing certain wave manipulations, by deriving the physics-compliant analytical formulation of the received signal at the receiver. We also introduce the numerical approximation of the signal for different operating regimes and different functionalities. Based on the obtained result, we study the impact of the number of fixed-size tiles and partitioning of a fixed-size RIS on the maximum achievable intensity. The validity of our findings is confirmed through extensive simulation results.

Keywords: Reconfigurable intelligent surface, smart radio environment, multi-tile RIS, maximum achievable intensity.

I. INTRODUCTION

Future wireless networks are expected to support very high data rates [1]. Between 2020 and 2030, data traffic from the global Internet Protocol (IP) is expected to increase by 55% each year, reaching 5,016 exabytes, while having to provide heterogeneous services [2], [3].

To meet these challenging demands, the concept of smart radio environment (SRE) is proposed [4], in which the wireless environment between communicating devices is seen no longer as a limitation, but as a variable that can be controlled through the use of reconfigurable intelligent surface (RIS) [5, 6]. In simple terms, RIS is an electromagnetic-based structure capable of modifying the impinging radio waves according to the specified objective and can be reconfigured after the fabrication. Typically, an RIS is constructed from a metasurface comprising elementary components, or unit cells, with dimensions and inter-element spacing significantly smaller than the operating wavelength [7]. Therefore, the RIS can be modeled as a continuous surface, which simplifies the underlying performance analysis and makes it more tractable for both theoretical studies and practical implementations [8].

One of the most important research issues to unlock the maximum performance of RIS lies in accurately formulating the received signal resulting from radio waves incident on the RIS from the transmitter. This formulation must balance precision with simplicity to

allow a clear analysis of the effects of typical system parameters on overall performance [9]. In [10], physics-consistent free-space pathloss models for RIS-assisted communications for different operating regimes are proposed and the impact of parameters such as the RIS size, transmission distances, and operating frequency on the received signal power at the receiver are revealed. These insights are essential to design more efficient and optimized RIS-based communication systems.

In most works in the literature, the RIS is seen as a single large surface. In practice, however, it can be more beneficial to partition the RIS into several groups, each of which performs a certain operation. In practice, however, it can be more beneficial to partition the RIS into several groups, each of which performs a certain operation. This partitioning technique improves the performance and adaptability of RIS, particularly in situations where frequency or geographic diversity are required. We may better adjust to the changing requirements of dynamic communication environments by splitting the RIS into subarrays, each of which is optimized for a certain function, such as beamforming, scattering, or absorption. We may better adjust to the changing requirements of dynamic communication environments by splitting the RIS into subarrays, each of which is optimized for a certain function, such as beamforming, scattering, or absorption. This will finally allow us to fully utilize RIS technology [11], [12].

* Corresponding Author.

Email: danufane@gmail.com

Received: November 05, 2024 ; Revised : November 22, 2024

Accepted: December 21, 2024 ; Published: December 31, 2024

Open access under CC-BY-NC-SA

© 2024 BRIN

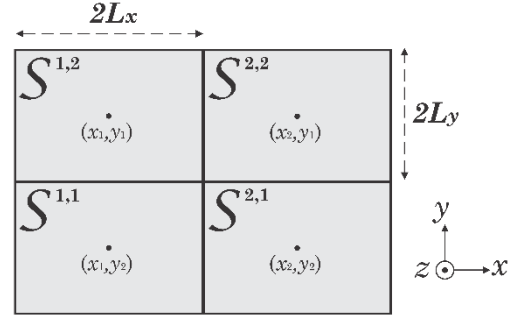
In [13] the authors derived the optimal reflection coefficients of an RIS containing several tiles that maximize the ergodic spectral efficiency. However, they consider only a sparsely deployed tile instead of a compact one and neglect the impact of the number of partitions of a fixed-sized RIS. However, they consider only a sparsely deployed tile instead of a compact one and neglect the impact of the number of partitions of a fixed-sized RIS.

In this paper, we investigate the performance of an RIS that consists of multiple tiles that can perform certain functions. In this paper, we investigate the performance of an RIS that consists of multiple tiles that can perform certain functionalities. We first derive the general formulation of the signal received by a receiver in space as a result of reflection by the RIS. We then consider two different functionalities that can be performed by the RIS. For each regime and functionality, we derive the closed-form approximation of the received signal and determine the condition under which the signal intensity is maximum. We also investigate the impact of the number of tiles as well as the number of partitions of a fixed-sized RIS towards the maximum intensity.

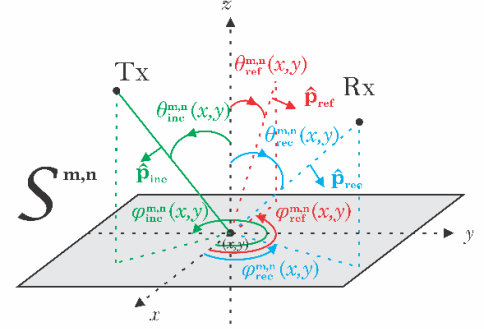
II. SYSTEM MODEL

We consider a system consisting of a transmitter (T_x), a receiver (R_x), and an RIS consisting of $M \times N$ tiles made of metasurface that coincide with the xy plane (i.e., $z = 0$) (see Figure 1). We consider a system consisting of a transmitter (T_x), a receiver (R_x), and an RIS consisting of $M \times N$ tiles made of metasurface that coincide with the xy plane (i.e., $z = 0$) (see Figure 1). For $m \in \{1, 2, \dots, M\}$ and $n \in \{1, 2, \dots, N\}$, we refer to the (m, n) -th tile as $S^{m,n}$.

Each $S^{m,n}$ has the size of $2L_x \times 2L_y$ and its center is located at $x_m \hat{x} + y_n \hat{y}$. We define the RIS as the union of all tiles, i.e.,



(a)



(b)

Figure 1. System model with multiple RISs; (a) top view of the 2×2 RIS, (b) notations and variables associated with the geometry of the RIS.

$$\mathcal{S} = \cup_{m,n} S^{m,n}$$

and we denote the location of the center of \mathcal{S} as $x_0 \hat{x} + y_0 \hat{y}$. For any point $\mathbf{s} = x \hat{x} + y \hat{y} \in \mathcal{S}^{m,n}$, the distances from T_x to \mathbf{s} and from \mathbf{s} to R_x are denoted as $d_{T_x}(x, y)$ and $d_{R_x}(x, y)$, respectively.

We denote,

TABLE 1.

SHORTHAND NOTATIONS ARE USED THROUGHOUT THE PAPER. SHORTHAND NOTATIONS ARE USED THROUGHOUT THE PAPER

Shorthand notation	Definition
$g(x, y) \Big _{x=x_1, y=y_1}^{x=x_2, y=y_2}$	$g(x_2, y_2) - g(x_2, y_1) - g(x_1, y_2) + g(x_1, y_1)$
$D_x^{m,n}$	$\sin \theta_{inc}^{m,n} \cos \varphi_{inc}^{m,n} + \sin \theta_{rec}^{m,n} \cos \varphi_{rec}^{m,n}$
$D_y^{m,n}$	$\sin \theta_{inc}^{m,n} \sin \varphi_{inc}^{m,n} + \sin \theta_{rec}^{m,n} \sin \varphi_{rec}^{m,n}$
D_x^0	$\sin \theta_{inc0} \cos \varphi_{inc0} + \sin \theta_{rec0} \cos \varphi_{rec0}$
D_y^0	$\sin \theta_{inc0} \sin \varphi_{inc0} + \sin \theta_{rec0} \sin \varphi_{rec0}$
$\Omega_{ref}^{m,n}(x, y; \tilde{\mathbf{p}}_{ref}, \tilde{\mathbf{p}}_{rec})$	$\frac{k^2}{\epsilon_0} p_{dm} \epsilon_{ref}^{m,n} (\tilde{\mathbf{p}}_{inc}, \tilde{\mathbf{p}}_{ref}) (\tilde{\mathbf{p}}_{rec} \cdot \tilde{\mathbf{p}}_{ref} - (\hat{\mathbf{S}}_{T_x}(x, y) \cdot \tilde{\mathbf{p}}_{rec}) (\hat{\mathbf{S}}_{T_x}(x, y) \cdot \tilde{\mathbf{p}}_{ref}))$
Ω_{ref0}	$\left(\frac{k^2}{\epsilon_0}\right) p_{dm} \epsilon_{ref} (\tilde{\mathbf{p}}_{inc}, \tilde{\mathbf{p}}_{ref}) (\tilde{\mathbf{p}}_{rec} \cdot \tilde{\mathbf{p}}_{ref} - (\hat{\mathbf{S}}_{T_x}(x_0, y_0) \cdot \tilde{\mathbf{p}}_{rec}) (\hat{\mathbf{S}}_{T_x}(x_0, y_0) \cdot \tilde{\mathbf{p}}_{ref}))$
$\sum_{m,n} (\cdot)$	Shorthand for $\sum_{m=1}^M \sum_{n=1}^N (\cdot)$

$$\begin{aligned} d_{T_x}^{m,n} &= d_{T_x}(x_m, y_n) \\ d_{R_x}^{m,n} &= d_{R_x}(x_m, y_n) \end{aligned}$$

i.e., $d_{T_x}^{m,n}$ and $d_{R_x}^{m,n}$ are the distances of T_x and R_x , respectively, from the center of $\mathcal{S}^{m,n}$. We also denote $d_{T_x0} = d_{T_x}(x_0, y_0)$ and $d_{R_x0} = d_{R_x}(x_0, y_0)$, i.e., d_{T_x0} and d_{R_x0} are the distances of T_x and R_x , respectively, from the center of \mathcal{S} .

The polar and azimuth angles of the incident wave at \mathbf{s} are denoted by $\theta_{\text{inc}}(x, y)$ and $\varphi_{\text{inc}}(x, y)$, respectively, while the polar and azimuth angles of the received wave at \mathbf{s} are denoted $\theta_{\text{rec}}(x, y)$ and $\varphi_{\text{rec}}(x, y)$, respectively. The polar and azimuth angles with respect to the center of $\mathcal{S}^{m,n}$ and \mathcal{S} are

$$\begin{aligned} \theta_Q^{m,n} &= \theta_Q(x_m, y_n), \\ \varphi_Q^{m,n} &= \varphi_Q(x_m, y_n), \\ \theta_{Q0} &= \theta_Q(x_0, y_0), \\ \varphi_{Q0} &= \varphi_Q(x_0, y_0), \end{aligned}$$

respectively, with $Q = \text{inc}$ for the incident wave and $Q = \text{rec}$ for the reflected wave.

Each point $\mathbf{s} \in \mathcal{S}^{m,n}$ is modeled as a reflection coefficient:

$$\Gamma_{\text{ref}}^{m,n}(x, y) = |\Gamma_{\text{ref}}^{m,n}(x, y)| \exp(j\Phi^{m,n}(x, y)) \quad (1)$$

$$\begin{aligned} \mathbf{E}(\mathbf{r}_{R_x}) \cdot \mathbf{p}_{\text{rec}} &\approx \mathbf{p}_{\text{rec}} \cdot \mathbf{E}_{0,\text{inc}}(\mathbf{r}_{R_x}; \mathbf{p}_{\text{inc}}) G(\mathbf{r}_{R_x}, \mathbf{r}_{T_x}) + F_R(\mathbf{r}_{R_x}) \\ F_R(\mathbf{r}_{R_x}) &= \sum_{m=1}^M \sum_{n=1}^N \int_{y_n-L_y}^{y_n+L_y} \int_{x_m-L_x}^{x_m+L_x} \mathcal{J}_R^{m,n}(x, y) e^{-jk\mathcal{P}_R^{m,n}(x,y)} dx dy \end{aligned}$$

$$\mathcal{P}_R^{m,n}(x, y) = d_{T_x}(x, y) + d_{R_x}(x, y) - (\phi_{\text{rec}} + \phi_{\text{ref}} + \Phi^{m,n}(x, y) + \pi \mathbb{1}_{\Omega_{\text{ref}}^{m,n}(x,y;\hat{\mathbf{p}}_{\text{ref}},\hat{\mathbf{p}}_{\text{rec}}) < 0})/k$$

$$\mathcal{J}_R^{m,n}(x, y) = \frac{|\Omega_{\text{ref}}^{m,n}(x,y;\mathbf{p}_{\text{ref}},\mathbf{p}_{\text{rec}})|}{d_{T_x}(x,y)d_{R_x}(x,y)} (\cos \theta_{\text{inc}}(x, y) + \cos \theta_{\text{rec}}(x, y)) \quad (2)$$

where $|\Gamma_{\text{ref}}^{m,n}(x, y)| \in \mathbb{R}^+$ and $\Phi^{m,n}(x, y)$ denote the amplitude and the phase of the reflection coefficient, respectively, at the point, (x, y) , denote the amplitude and the phase of the reflection coefficient, respectively, at the point, (x, y) . In this paper, we assume that

$$|\Gamma_{\text{ref}}^{m,n}(x, y)| = 1 \quad (3)$$

for all $(m, n) \in \{1, \dots, M\} \times \{1, \dots, N\}$. We refer to [10] for the definition of the other notation used in this paper. The definitions of some short-hand expressions are given in Table 1.

A system with a single tile can be classified into an electrically large regime or an electrically small regime depending on the size of the tile and the T_x and R_x distances from the tile [10]. For a system with multiple tiles, we introduce the following two regimes of system operation.

Definition 1. *The system is said to operate in the near field if each $\mathcal{S}^{m,n}$ is in the electrically large regime.*

Meanwhile, the system is said to operate in the far field if each $\mathcal{S}^{m,n}$ is in the electrically small regime and the following approximations hold for $\mathbf{P} \in \{\text{inc}, \text{rec}\}$, $\mathbf{Q} \in \{T_x, R_x\}$, and for all $(x, y) \in \mathcal{S}$:

$$\begin{aligned} (i) \quad & \sin \theta_{\mathbf{P}}(x, y) \approx \sin \theta_{\mathbf{P}0}, \\ (ii) \quad & d_{\mathbf{Q}}(x, y) \approx d_{\mathbf{Q}0} \end{aligned}$$

III. RECEIVED ELECTRIC FIELD FORMULATION

Based on the assumptions given in Section II, the electric field received at R_x and projected into the receive polarization of the R_x antenna in the presence of multile RIS is given as follows.

Lemma 1. *Let $\mathbf{1}_{(\cdot)}$ be the indicator function and $\mathcal{J}_0 = jk/(16\pi^2)$. In presence of a dipole T_x antenna with transmit polarization $\hat{\mathbf{p}}_{\text{inc}}$ and \mathcal{S} with reflect polarization $\hat{\mathbf{p}}_{\text{ref}}$ the electric field received at R_x and projected into $\hat{\mathbf{p}}_{\text{rec}}$ can be given by (2) at the top of this page. The definition of $\Omega_{\text{ref}}^{m,n}(x, y; \hat{\mathbf{p}}_{\text{ref}}, \hat{\mathbf{p}}_{\text{rec}})$ is given in Table 1.*

Proof. The proof follows by replacing \mathcal{S} with $\cup_{m,n} \mathcal{S}^{m,n}$ in [1, Theorem 2] and using similar steps in [1, Appendix E].

The received electric field in (2) is formulated as the

sum of the incident electric field in the absence of \mathcal{S} (the first term in the right-hand side) and the contribution due to the reflection from \mathcal{S} which we denote by $F_R(\mathbf{r}_{R_x})$.

Corollary 1. *The maximum value of $|F_R(\mathbf{r}_{R_x})|$ in (2) can be approximated as follows:*

$$|F_R(\mathbf{r}_{R_x})| \approx \iint_{\mathcal{S}} I_0 |I_R^{m,n}(x, y)| dx dy \quad (4)$$

In particular, $|F_R(\mathbf{r}_{R_x})|$ in (4) is achieved when the following holds for all $(m_1, n_1), (m_2, n_2) \in \{1, \dots, M\} \times \{1, \dots, N\}$ and for all $(x_1, y_1) \in \mathcal{S}^{m_1, n_1}, (x_2, y_2) \in \mathcal{S}^{m_2, n_2}$:

$$\begin{aligned} & \Phi^{m_1, n_1}(x_1, y_1) - k \left(d_{T_x}(x_1, y_1) + d_{R_x}(x_1, y_1) \right) \\ & \quad + \pi \mathbb{1}_{\Omega_{\text{ref}}^{m_1, n_1}(x_1, y_1; \hat{\mathbf{p}}_{\text{ref}}, \hat{\mathbf{p}}_{\text{rec}}) < 0} \\ & = \Phi^{m_2, n_2}(x_2, y_2) - k \left(d_{T_x}(x_2, y_2) + d_{R_x}(x_2, y_2) \right) \\ & \quad + \pi \mathbb{1}_{\Omega_{\text{ref}}^{m_2, n_2}(x_2, y_2; \hat{\mathbf{p}}_{\text{ref}}, \hat{\mathbf{p}}_{\text{rec}}) < 0} \end{aligned} \quad (5)$$

Proof. Note that $I_R^{m,n}(x,y)$ in (2) is real-valued for all $(m,n) \in \{1, \dots, M\} \times \{1, \dots, N\}$. Therefore, according to the triangle inequality for summation and integration, $|F_R(\mathbf{r}_{\text{Rx}})|$ in (2) is maximized when $\mathcal{P}_R^{m_1, n_1}(x_1, y_1) = \mathcal{P}_R^{m_2, n_2}(x_2, y_2)$ for all $(m_1, n_1), (m_2, n_2) \in \{1, \dots, M\} \times \{1, \dots, N\}$ and for all $(x_1, y_1) \in S^{m_1, n_1}, (x_2, y_2) \in S^{m_2, n_2}$. This condition is equivalent to (5). In this case, the maximum value of $|F_R(\mathbf{r}_{\text{Rx}})|$ in (2) is given by (4).

Remark 1. From (4), we see that the intensity of the reflected field depends only on the total area of the RIS and is invariant under any partitioning of the RIS. We also note that the maximum intensity increases with the number of tiles, provided that the area of each tile is fixed. However, this does not imply that the intensity goes to infinity when the RIS size goes to infinity, as shown by the following corollary.

Corollary 2. Suppose that $d_{P_1}(x,y) \leq d_{P_2}(x,y)$ for all $(x,y) \in S$ and $\exists(P_1, P_2) = \{(\mathbf{T}_x, \mathbf{R}_x), (\mathbf{R}_x, \mathbf{T}_x)\}$. Let us define,

$$C_{\text{ref}} = (2k^3 p_{\text{dm}} \varepsilon(\hat{\mathbf{p}}_{\text{inc}}, \hat{\mathbf{p}}_{\text{ref}})) / (16\pi^2 \epsilon_0) \quad (6)$$

then, $|F_R(\mathbf{r}_{\text{Rx}})|$ is upper bounded by,

$$|F_R(\mathbf{r}_{\text{Rx}})| \leq 2\pi C_{\text{ref}}(1 + z_{P_2}/z_{P_1}) \quad (7)$$

Proof. The upper bound for a single tile is given by the proof of Corollary 6 in [10]. The proof follows by extending the analysis to multiple tiles.

Lemma 1 and Corollary 1 are given for a general functionality of S which depends on $\Phi^{m,n}(x,y)$. In the following subsections, we consider two different functionalities of S .

A. S configured as a hybrid reflector

In this section, we analyze the case study in which S operates as a hybrid reflector. This functionality is obtained when the following holds for each (m,n) :

$$\Phi^{m,n}(x,y) = k(\alpha_R^{m,n}x + \beta_R^{m,n}y) + \phi_0^{m,n} \quad (8)$$

where $\phi_0^{m,n} \in [0, 2\pi]$ is a fixed phase shift introduced by $S^{m,n}$ while $\alpha_R^{m,n} \in \mathbb{R}$ and $\beta_R^{m,n} \in \mathbb{R}$ are design parameters that can be configured such that the direction of the wave reflected by each tile $S^{m,n}$ is towards Rx. It is worth noting that $\alpha_R^{m,n}$ and $\beta_R^{m,n}$ are generally not constant over all $S^{m,n}$; they depend on the direction of Tx and Rx with respect to each $S^{m,n}$.

Corollary 3. For each $(m,n) \in S^{m,n}$, let $(x_s^{m,n}, y_s^{m,n})$ be the unique solution of the following system of equations:

$$\begin{aligned} \frac{x_s^{m,n} - x_{\text{Tx}}}{d_{\text{Tx}}(x_s^{m,n}, y_s^{m,n})} - \frac{x_{\text{Rx}} - x_s^{m,n}}{d_{\text{Rx}}(x_s^{m,n}, y_s^{m,n})} &= \alpha_R^{m,n}, \\ \frac{y_s^{m,n} - y_{\text{Tx}}}{d_{\text{Tx}}(x_s^{m,n}, y_s^{m,n})} - \frac{y_{\text{Rx}} - y_s^{m,n}}{d_{\text{Rx}}(x_s^{m,n}, y_s^{m,n})} &= \beta_R^{m,n}. \end{aligned} \quad (9)$$

For $Q \in \{\text{inc}, \text{rec}\}$, let us denote $\Theta_Q^{m,n} = \theta_Q(x_s^{m,n}, y_s^{m,n})$ and $\Phi_Q = \varphi_Q(x_s^{m,n}, y_s^{m,n})$. In the near field $F_R(\mathbf{r}_{\text{Rx}})$ is approximated by (6) at the top of this page where we define,

$$\begin{aligned} \mathcal{P}_R^{m_1, n_1} &= d_{\text{Tx}}(x_s^{m,n}, y_s^{m,n}) + d_{\text{Rx}}(x_s^{m,n}, y_s^{m,n}) \\ &\quad - (\alpha_R^{m,n}x_s^{m,n} + \beta_R^{m,n}y_s^{m,n}) \\ &\quad - (\phi_0^{m,n} + \phi_{\text{ref}} + \phi_{\text{rec}} \\ &\quad + \pi \mathbb{1}_{\Omega_{\text{ref}}^{m,n}(x_s^{m,n}, y_s^{m,n}, \hat{\mathbf{p}}_{\text{ref}}, \hat{\mathbf{p}}_{\text{rec}}) < 0}) / k \end{aligned}$$

and

$$\begin{aligned} K_1^{m,n} &= (\mathcal{R}_1^{m,n} + \mathcal{R}_3^{m,n}/2) / \left(\sqrt{\mathcal{R}_1^{m,n} + \mathcal{R}_2^{m,n} + \mathcal{R}_3^{m,n}} \right), \\ K_2^{m,n} &= (\mathcal{R}_2^{m,n} + \mathcal{R}_3^{m,n}/2) / \left(\sqrt{\mathcal{R}_1^{m,n} + \mathcal{R}_2^{m,n} + \mathcal{R}_3^{m,n}} \right) \end{aligned}$$

where $\mathcal{R}_1^{m,n}, \mathcal{R}_2^{m,n}, \mathcal{R}_3^{m,n}$ are given in (7).

Proof. For given $(m,n) \in \{1, \dots, M\} \times \{1, \dots, N\}$, the stationary points of $\mathcal{P}_R^{m,n}(x,y)$ in (2) correspond to the solutions of (9). Due to the monotonicity of (9) with respect to $x_s^{m,n}$ and $y_s^{m,n}$, either one or no stationary point exist at each $S^{m,n}$. The contribution $S^{m,n}$ that contains a stationary point $(x_s^{m,n}, y_s^{m,n})$ is given by [1, Corollary 3 and 4]. Meanwhile, the contribution from $S^{m,n}$ that does not contain $(x_s^{m,n}, y_s^{m,n})$ is given by [1, Lemma 5]. The proof follows aggregating the contribution from all $S^{m,n}$.

Remark 2. Assume that, for all

$$(m,n) \in \{1, \dots, M\} \times \{1, \dots, N\},$$

we have $\alpha_R^{m,n} = -\mathcal{D}_x^{m,n}$ and $\beta_R^{m,n} = -\mathcal{D}_y^{m,n}$, where the definitions of $\mathcal{D}_x^{m,n}$ and $\mathcal{D}_y^{m,n}$ are given in Table I. From (9) we can see that, in this case, a stationary point is guaranteed to exist at the center of each $S^{m,n}$, i.e., $(x_s^{m,n}, y_s^{m,n}) = (x_m, y_n) \in S^{m,n}$. Thus, according to (6), $F_R(\mathbf{r}_{\text{Rx}})$ can be approximated as

$$F_R(\mathbf{r}_{\text{Rx}}) \approx \sum_{m=1}^M \sum_{n=1}^N \frac{|\Omega_{\text{ref}}^{m,n}(x_m, y_n)| e^{-jk\rho_{R,S}^{m,n}}}{8\pi(K_1^{m,n}d_{\text{Tx}} + K_2^{m,n}d_{\text{Rx}})} \quad (10)$$

Since $K_1^{m,n}, K_2^{m,n}, d_{\text{Tx},S}^{m,n}, d_{\text{Rx},S}^{m,n} > 0$ for all (m,n) , $|F_R(\mathbf{r}_{\text{Rx}})|$ in (10) is maximized when the following holds for all $(m_1, n_1), (m_2, n_2) \in \{1, \dots, M\} \times \{1, \dots, N\}$:

$$\begin{aligned} kg^{m_1, n_1} - \phi_0^{m_1, n_1} - \pi \mathbb{1}_{(\Omega_{\text{ref}}^{m_1, n_1}(x_s^{m_1, n_1}, y_s^{m_1, n_1}) < 0)} \\ = kg^{m_2, n_2} - \phi_0^{m_2, n_2} - \pi \mathbb{1}_{(\Omega_{\text{ref}}^{m_2, n_2}(x_s^{m_2, n_2}, y_s^{m_2, n_2}) < 0)} \end{aligned} \quad (11)$$

where we define

$$g^{m,n} = d_{\text{Tx}}^{m,n} + d_{\text{Rx}}^{m,n} - \alpha_R^{m,n}x_m - \beta_R^{m,n}y_n$$

Furthermore, when each $S^{m,n}$ is optimized according to (11), $F_R(\mathbf{r}_{\text{Rx}})$ increases with the number of tiles, i.e., M and N , provided that each $S^{m,n}$ is still in the electrically large regime.

Corollary 4. In the far field, $F_R(\mathbf{r}_{Rx})$ can be given as

$$F_R(\mathbf{r}_{Rx}) \approx \frac{jkL_x L_y (\cos \theta_{inc0} + \cos \theta_{rec0})}{4\pi^2 d_{Tx0} d_{Rx0}} \times \sum_{m,n} (|\Omega_{ref0}| \text{sinc}(kL_x \mathcal{D}_{\alpha_R}^{m,n}) \text{sinc}(kL_y \mathcal{D}_{\beta_R}^{m,n}) e^{-jk\mathcal{D}_{R0}^{m,n}}) \quad (12)$$

where the definition of Ω_{ref0} is given in Table 1 and we define

$$\mathcal{D}_{\alpha_R}^{m,n} = \mathcal{D}_x^{m,n} + \alpha_R^{m,n}, \mathcal{D}_{\beta_R}^{m,n} = \mathcal{D}_y^{m,n} + \beta_R^{m,n},$$

and

$$\mathcal{P}_{R0}^{m,n} = g^{m,n} - \left(\phi_0^{m,n} + \phi_{ref} + \phi_{rec} + \pi \mathbb{1}_{\Omega_{ref}^{m_2, n_2}(x,y; \hat{\mathbf{p}}_{ref}, \hat{\mathbf{p}}_{rec}) < 0} \right) / k.$$

Proof. Let $F_R^{m,n}(\mathbf{r}_{Rx})$ be the contribution from $\mathcal{S}^{m,n}$ that is configured for anomalous reflection in the electrically small regime towards $F_R(\mathbf{r}_{Rx})$. The approximation of $F_R(\mathbf{r}_{Rx})$ is given by [1, Corollary 5]:

$$F_R(\mathbf{r}_{Rx}) \approx \frac{jk\Omega_{ref0}^{m,n} L_x L_y (\cos \theta_{inc}^{m,n} + \cos \theta_{rec}^{m,n})}{4\pi^2 d_{Tx}^{m,n} d_{Rx}^{m,n}} e^{-jk\mathcal{D}_{R0}^{m,n}} \text{sinc}(kL_x \mathcal{D}_{\alpha_R}^{m,n}) \text{sinc}(kL_y \mathcal{D}_{\beta_R}^{m,n}) \quad (13)$$

where denote

$$\Omega_{ref0}^{m,n} = \Omega_{ref}^{m,n}(x_m, y_n; \hat{\mathbf{p}}_{ref}, \hat{\mathbf{p}}_{rec}).$$

From Definition 1, in the far field, we have

$$\begin{aligned} d_{Tx}^{m,n} &\approx d_{Tx0}, \\ d_{Rx}^{m,n} &\approx d_{Rx0}, \\ \cos \theta_{inc}^{m,n} &\approx \cos \theta_{inc0}, \\ \cos \theta_{rec}^{m,n} &\approx \cos \theta_{rec0} \end{aligned}$$

for all $(m,n) \in \{1, \dots, M\} \times \{1, \dots, N\}$. We also have $\hat{\mathbf{s}}_{Tx}(x_m, y_n) \approx \hat{\mathbf{s}}_{Tx}(x_0, y_0)$ which implies $\Omega_{ref0}^{m,n} \approx \Omega_{ref0}$. The proof follows from applying these approximations to (13) and aggregating the contribution from all tiles.

Remark 3. Due to triangle inequality $|F_R(\mathbf{r}_{Rx})|$ in (12) is maximized when the following hold:

$$\begin{aligned} \mathcal{P}_{R0}^{m_1, n_1} &= \mathcal{P}_{R0}^{m_2, n_2}, \\ \alpha_R^{m,n} &= -\mathcal{D}_x^{m,n}, \\ \beta_R^{m,n} &= -\mathcal{D}_y^{m,n} \end{aligned} \quad (14)$$

When (14) applies, $|F_R(\mathbf{r}_{Rx})|$ in the far field is given as

$$|F_R(\mathbf{r}_{Rx})| = \frac{k\mathcal{A}_S \Omega_{ref0} (\cos \theta_{inc0} + \cos \theta_{rec0})}{16\pi^2 d_{Tx0} d_{Rx0}} \quad (15)$$

where is the total area of \mathcal{S} . Thus, we evince that $|F_R(\mathbf{r}_{Rx})|$ is invariant under different partitioning of \mathcal{S} . Also, $|F_R(\mathbf{r}_{Rx})|$ increases with the area of \mathcal{S} , provided that the system is still operating in the far field.

B. S configured as a Beamformer

In this subsection, we analyze the case study in which \mathcal{S} operates as a beamformer. This functionality is obtained when the following holds for each (m,n) :

$$\Phi^{m,n}(x,y) = k(d_{Tx}(x,y) + d_{Rx}(x,y)) + \phi_0^{m,n} \quad (16)$$

Unlike $\Phi^{m,n}(x,y)$ in (8) which depends on the direction of Tx and Rx with respect to $\mathcal{S}^{m,n}$, $\Phi^{m,n}(x,y)$ in (16) depends on the distance of Rx with respect to each point in $\mathcal{S}^{m,n}$.

Corollary 5. When \mathcal{S} is configured as a beamformer, $F_R(\mathbf{r}_{Rx})$ can be given as

$$F_R(\mathbf{r}_{Rx}) \approx \frac{jk}{16\pi^2} \iint_{\mathcal{S}} \frac{|\Omega_{ref}^{m,n}(x,y; \mathbf{p}_{ref}, \mathbf{p}_{rec})| e^{j\phi_R^{m,n}(x,y)}}{d_{Tx}(x,y) d_{Rx}(x,y)} \times (\cos \theta_{inc}(x,y) + \cos \theta_{rec}(x,y)) dx dy \quad (17)$$

where we define

$$\phi_R^{m,n}(x,y) = \phi_{rec} + \phi_{ref} + \phi_0^{m,n} + \pi \mathbb{1}_{\Omega_{ref}^{m,n}(x,y; \hat{\mathbf{p}}_{ref}, \hat{\mathbf{p}}_{rec}) < 0}$$

Proof. The contribution from a tile that is configured for beamforming is given by [1, Eq.(33)]. The proof follows from aggregating the contribution from all tiles.

As shown in [10], a tile $\mathcal{S}^{m,n}$ configured for beamforming is typically operating in the electrically small regime. Therefore, we consider only the approximation of $F_R(\mathbf{r}_{Rx})$ in the far field.

Corollary 6. In the far field, $F_R(\mathbf{r}_{Rx})$ can be given as

$$F_R(\mathbf{r}_{Rx}) \approx \frac{jk\mathcal{A}_S \Omega_{ref0} (\cos \theta_{inc0} + \cos \theta_{rec0})}{16\pi^2 d_{Tx0} d_{Rx0}} \iint_{\mathcal{S}} e^{j\phi_R^{m,n}(x,y)} dx dy \quad (18)$$

Proof. It is similar to the proof of Corollary 4.

Remark 4. From (17) and (18), we demonstrate the following.

Assume that each $\phi_0^{m,n}$ is configured such that

$$\begin{aligned} &\phi_0^{m_1, n_1} + \pi \mathbb{1}_{\Omega_{ref}^{m_1, n_1}(x,y; \hat{\mathbf{p}}_{ref}, \hat{\mathbf{p}}_{rec}) < 0} \\ &= \phi_0^{m_2, n_2} + \pi \mathbb{1}_{\Omega_{ref}^{m_2, n_2}(x,y; \hat{\mathbf{p}}_{ref}, \hat{\mathbf{p}}_{rec}) < 0} \end{aligned} \quad (19)$$

For all $(m_1, n_1), (m_2, n_2) \in \{1, \dots, M\} \times \{1, \dots, N\}$. In this case, we have $\phi_R^{m_1, n_1}(x,y) = \phi_R^{m_2, n_2}(x,y)$ and thus the intensity of $F_R(\mathbf{r}_{Rx})$ in (17) is equivalent to (4), which

the maximum achievable intensity by \mathcal{S} . Therefore, an RIS configured as a beamformer is the most optimal configuration in terms of the received signal.

If (19) is satisfied, in the far field, the maximum intensity of the electric field in (18) is given as

$$F_R(\mathbf{r}_{Rx}) \approx \frac{k\omega A_S \Omega_{\text{ref0}} (\cos \theta_{\text{inc0}} + \cos \theta_{\text{rec0}})}{16\pi^2 d_{Tx0} d_{Rx0}} \quad (20)$$

IV. NUMERICAL RESULTS

In this section, we illustrate some numerical examples in order to validate our results. Unless stated otherwise, parameters specified in Table II are used throughout the section. It is worth mentioning that, under these parameters, the RIS is always optimized to achieve the maximum achievable intensity at Rx for its configuration and operating regime of interest.

A. Impact of Distances

Figure 2 shows the intensity plot as a function of the distances Tx and Rx. As shown in the figure, an RIS configured as a hybrid reflector can be approximated by two different operating regimes; the near-field and far-field. Meanwhile, when the RIS is configured as a beamformer, it is typically operating in the far field. We also observe that the analytical approximations obtained for the near-field and far-field spectroscopy due to an RIS configured as a hybrid reflector overlap with the integral representation for their respective regimes of interest.

B. Impact of number of tiles

Figure 3 shows the plot of intensity as a function of the number of tiles (i.e., $M \times N$) where the distances of Tx and Rx to the center of the RIS is $d_{Tx0} = d_{Rx0} = d_0 = \{5, 100\}$ m, which represents the near and far fields. From Figure 3, we can see that both in the near- and far-field, the intensity generally increases with the number of tiles. However, the intensity is always upper bounded by a finite value as the number of tiles goes to infinity. We also see that in the near field, the intensity of an RIS configured as a beamformer is much higher than that of an RIS configured as a hybrid reflector. Meanwhile, in the far field, the intensities are approximately the same.

C. Impact of the number of partitions

Figure 4 shows the plot of intensity as a function of the number of partitions in which $5\text{m} \times 5\text{m}$ RIS is

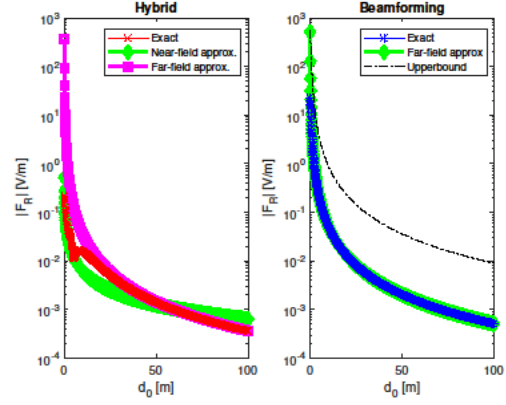


Figure 2. Intensity of the signal received at the receiver versus distance from the Tx and Rx to the RIS. Setup: $d_{Tx0} = d_{Rx0} = d_0$, $M = N = 2$, $2L_x = 2L_y = 0.5$ m

partitioned into $M \times N$ tiles where $M = N$. From the figure we can see that, when the RIS is configured as a hybrid reflector, the intensity increases with the number of partitions up to a certain point. Past this point, the intensity is invariant to the number of partitions. Meanwhile, when the RIS is configured as a beamformer, the intensity is invariant under the number of partitions.

V. CONCLUSIONS

In this paper, we have investigated the performance of an RIS made of multiple tiles of metasurface by

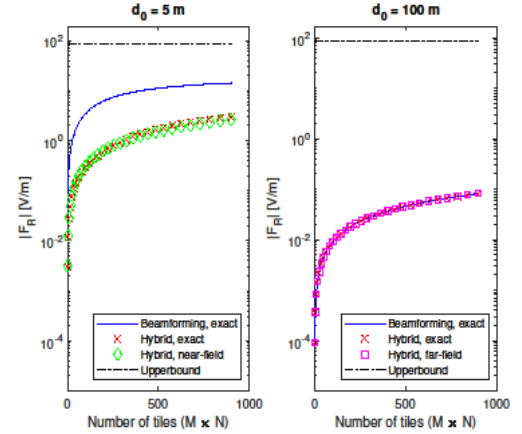


Figure 3. Intensity vs. number of tiles. Setup: $d_{Tx0} = d_{Rx0} = d_0$, $M = N$, $2L_x = 2L_y = 0.5$ m

TABLE 2.
SIMULATION SETUP

Settings
$f = 28$ GHz, $\lambda = 10.71$ mm
$\epsilon_0 = 8.85 \cdot 10^{-12}$ Farad/meter
$p_{\text{dm}} = (k^2 / \epsilon_0)^{-1}$
$\hat{\mathbf{p}}_{\text{inc}} = \hat{\mathbf{p}}_{\text{ref}} = \hat{\mathbf{p}}_{\text{rec}} = \hat{\mathbf{y}}$
$\phi_0 = \phi_{\text{inc}} = \phi_{\text{ref}} = \phi_{\text{rec}} = 0$
$\epsilon(\hat{\mathbf{p}}_{\text{inc}}, \hat{\mathbf{p}}_{\text{ref}}) = 1$
$\theta_{\text{inc0}} = \pi/6, \phi_{\text{inc0}} = \pi/4$
$\theta_{\text{rec0}} = \pi/4, \phi_{\text{rec0}} = 5\pi/4$
$(x_0, y_0) = (0, 0), d_{Tx0} = d_{Rx0} = d_0$
$2L_x = 2L_y = 0.5\text{m}, M = N = 2$
$\alpha_R^{m,n} = -\mathcal{D}_x^{m,n}, \beta_R^{m,n} = -\mathcal{D}_y^{m,n}$

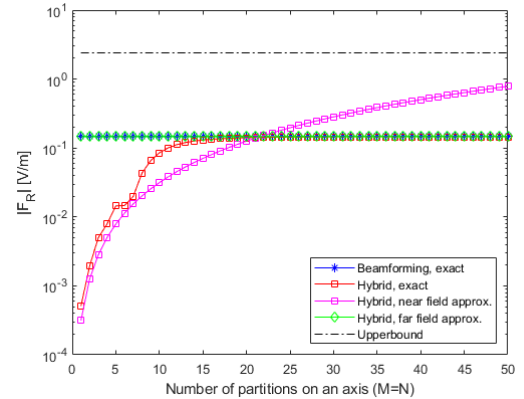


Figure 4. Intensity of the received signal at the receiver vs. number of RIS partitions. Setup: $M \times 2L_x = N \times 2L_y = 5$ m, $d_{Tx0} = d_{Rx0} = d_0 = 50$ m.

deriving the analytical formulation for the received electric field at Rx and obtaining the closed form approximations of the intensity for different functionalities and regimes. On the basis of the obtained results, we remarked on the performance trend of the RIS in terms of received field intensity as a function of relevant parameters. We validated our analytical results through numerical simulations.

DECLARATIONS

Conflict of Interest

The authors have declared that there are no competing interests.

CRedit Authorship Contribution

Fadil Habibi Danufane: Conceptualization, Methodology, Software, Validation, Formal Analysis, Writing - Original Draft; Ashif Aminulloh Fathnan: Writing - Review & Editing; R. Priyo Hartono Adji: Writing - Review & Editing, Funding Acquisition; Arie Setiawan: Writing - Review & Editing; Prasetyo Putranto: Writing - Review & Editing

Funding

The authors acknowledge the National Research and Innovation Agency (BRIN) for funding our research through the Rumah Program Purwarupa Sistem Pendukung Keputusan Analisis Citra Satelit 2024.

REFERENCES

- [1] S. Dang, O. Amin, B. Shihada, and M.-S. Alouini, "What should 6G be?" *Nat. Electron.*, vol. 3, no. 1, pp. 20–29, 2020, doi: 10.1038/s41928-019-0355-6.
- [2] A. Sufyan, K. B. Khan, O. A. Khashan, T. Mir, and U. Mir, "From 5G to beyond 5G: A comprehensive survey of wireless network evolution, challenges, and promising technologies," *Electronics*, vol. 12, no. 10, p. 2200, 2023, doi: <https://doi.org/10.3390/electronics12102200>.
- [3] M. Hosseinzadeh, A. Hemmati, and A. M. Rahmani, "6G-enabled internet of things: Vision, techniques, and open issues," *Comput. Model. Eng. Sci.*, vol. 133, no. 3, 2022, doi: 10.32604/cmesci.2022.021094.
- [4] M. Di Renzo *et al.*, "Smart radio environments empowered by reconfigurable AI meta-surfaces: An idea whose time has come," *EURASIP J. Wirel. Commun. Netw.*, vol. 2019, no. 1, pp. 1–20, 2019, doi: 10.1186/s13638-019-1438-9.
- [5] Q. Wu and R. Zhang, "Towards smart and reconfigurable environment: Intelligent reflecting surface aided wireless network," *IEEE Commun. Mag.*, vol. 58, no. 1, pp. 106–112, 2019, doi: <https://doi.org/10.1109/MCOM.001.1900107>.
- [6] C. Huang, A. Zappone, G. C. Alexandropoulos, M. Debbah, and C. Yuen, "Reconfigurable intelligent surfaces for energy efficiency in wireless communication," *IEEE Trans. Wirel. Commun.*, vol. 18, no. 8, pp. 4157–4170, 2019, doi: 10.1109/TWC.2019.2922609.
- [7] T. J. Cui, M. Q. Qi, X. Wan, J. Zhao, and Q. Cheng, "Coding metamaterials, digital metamaterials and programmable metamaterials," *Light. Sci. Appl.*, vol. 3, no. 10, e218-e218, 2014, doi: 10.1038/lsa.2014.99.
- [8] M. Najafi, V. Jamali, R. Schober, and H. V. Poor, "Physics-based modeling and scalable optimization of large intelligent reflecting surfaces," *IEEE Trans. Commun.*, vol. 69, no. 4, pp. 2673–2691, 2020, doi: 10.1109/TCOMM.2020.3047098.
- [9] W. Tang *et al.*, "Wireless communications with reconfigurable intelligent surface: Path loss modeling and experimental measurement," *IEEE Trans. Wirel. Commun.*, vol. 20, no. 1, pp. 421–439, 2020, doi: 10.1109/TWC.2020.3024887.
- [10] F. H. Danufane, M. Di Renzo, J. de Rosny, and S. Tretyakov, "On the path-loss of reconfigurable intelligent surfaces: An approach based on Green's theorem applied to vector fields," *IEEE Trans. Commun.*, vol. 69, no. 8, pp. 5573–5592, 2021, doi: 10.1109/TCOMM.2021.3081452.
- [11] M. Di Renzo *et al.*, "Smart radio environments empowered by reconfigurable intelligent surfaces: How it works, state of research, and the road ahead," *IEEE J. Sel. Areas Commun.*, vol. 38, no. 11, pp. 2450–2525, 2020, doi: 10.1109/JSAC.2020.3007211.
- [12] X. Guan, Q. Wu, and R. Zhang, "Joint power control and passive beamforming in IRS-assisted spectrum sharing," *IEEE Commun. Lett.*, vol. 24, no. 7, pp. 1553–1557, 2020, doi: 10.1109/LCOMM.2020.2979709.
- [13] W. Chen, X. Yang, S. Jin, and P. Xu, "Sparse array of sub-surface aided anti-blockage mmWave communication systems," in *GLOBECOM 2020-2020 IEEE Global Communications Conference*, pp. 1–6, doi: 10.1109/GLOBECOM42002.2020.9322466.